FULL PAPER

Magnetic Resonance in Medicine 00:00–00 (2016)

Fast 3D Ultrashort Echo-Time Spiral Projection Imaging Using Golden-Angle: A Flexible Protocol for In Vivo Mouse Imaging at High Magnetic Field

Charles R Castets,[1,2] William Lefrançois,[1,2] Didier Wecker,[3] Emeline J Ribot,[1,2] Aurélien J Trotier,[1,2] Eric Thiaudière,[1,2] Jean-Michel Franconi,[1,2] and Sylvain Miraux[1,2]*

Purpose: To develop a fast three-dimensional (3D) k-space encoding method based on spiral projection imaging (SPI) with an interleaved golden-angle approach and to validate this novel sequence on small animal models.

Methods: A disk-like trajectory, in which each disk contained spirals, was developed. The 3D encoding was performed by tilting the disks with a golden angle. The sharpness was first calculated at different T_2^* values. Then, the sharpness was measured on phantom using variable undersampling ratios. Finally, the sampling method was validated by whole brain time-of-flight angiography and ultrasmall superparamagnetic iron oxide (USPIO) enhanced free-breathing liver angiography on mouse.

Results: The in vitro results demonstrated the robustness of the method for short T_2^* and high undersampling ratios. In vivo experiments showed the ability to properly detect small vessels in the brain with an acquisition time shorter than 1 min. Free-breathing mice liver angiography showed the insensitivity of this protocol toward motions and flow artifacts, and enabled the visualization of liver motion during breathing.

Conclusions: The method implemented here allowed fast 3D k-space sampling with a high undersampling ratio. Combining the advantages of center-out spirals with the flexibility of the golden angle approach could have major implications for real-time imaging. **Magn Reson Med 000:000–000, 2016. © 2016 Wiley Periodicals, Inc.**

Key words: spiral; 3D; UTE; golden angle; 7T; self-gating; mouse

INTRODUCTION

First introduced by Ahn et al (1) and redefined by Meyer et al (2), spiral readout has been used during the past decades in humans and more recently in small animal imaging. Its use enables fast image acquisition with reduced motion and flow artifacts. Although spiral readout presents several limitations such as off resonance and magnet shimming sensitivity, it has been validated for applications such as functional MRI studies (3), coronary artery imaging (4), and most recently cardiac three-dimensional (3D) T_1 mapping on mice (5). The ability to cover a large part of the k-space after one excitation allows faster acquisitions of images in two or three dimensions. Indeed, several methods combining spiral readouts with 3D imaging have been developed. Among the existing techniques, the stack-of-spiral (SOS) approach allowed fast space encoding by stacking spiral planes in the slice direction. This method has been applied to free-breathing late gadolinium-enhanced experiments (6,7) and to sodium imaging at high magnetic field (8). The main advantages of the SOS approach are the reduced scan times and the ability to acquire anisotropic field of view (FOV). However, SOS suffers from several drawbacks such as the slightly longer echo time (TE) caused by the spatial encoding in the third direction, and the relative undersampling in the lower spatial frequencies when compared with 3D koosh-ball radial trajectories, for example. Several spiral-encoding methods were developed to oversample the center of the k-space. First, twisted projection imaging (TPI) (9) enables fast signal acquisition with limited T_2^* effect. TPI was used for sodium imaging in both cerebral tumors (10) and human articular cartilage (11). Close to TPI, the cones method (12) allows fast k-space coverage using variable density trajectory. The cones approach was used in similar applications as TPI, among which are sodium imaging of human patellar cartilage (13) and free-breathing 3D coronary artery imaging (14).

These space-encoding approaches (spiral, TPI, and cones) are compatible with an interleaved approach and may use a minimum time between the radiofrequency (RF) excitation and the signal acquisition, hence relevant for short and ultrashort echo time (UTE) imaging (15–17). Although these techniques are very efficient in imaging and quantifying sodium concentration in various organs, the flexibility and robustness for undersampling has not yet been assessed. Among the existing methods, the golden-angle approach is particularly efficient to achieve pseudo-random sampling of the k-space, and was used in numerous applications (18). Moreover, eddy current artifacts are significantly reduced (19) and it is adapted for sliding window reconstruction. Few

[1]Centre de Résonance Magnétique des Systèmes Biologiques, UMR5536 CNRS, Bordeaux, France.

[2]Centre de Résonance Magnétique des Systèmes Biologiques, UMR5536 Université de Bordeaux, Bordeaux, France.

[3]Bruker Biospin MRI GMBH, Ettlingen, Germany

Grant sponsor: French National Research Agency's Investments for the Future Program; Grant number: "NewFISP"; ANR- 10-LABX-57.

*Correspondence to: Sylvain Miraux, Ph.D., Centre de Résonance Magnétique des Systèmes Biologiques, UMR5536 CNRS, Bordeaux, France; 146 rue Léo Saignat 33076 Bordeaux Cedex. E-mail: miraux@rmsb.u-bordeaux2.fr

Received 20 January 2016; revised 11 April 2016; accepted 13 April 2016
DOI 10.1002/mrm.26263
Published online 00 Month 2016 in Wiley Online Library (wileyonlinelibrary.com).

© 2016 Wiley Periodicals, Inc.

examples of combinations of golden-angle and two-dimensional (2D) spiral readouts were proposed in the literature (20). As far as we know, no sequence combining ultrashort echo time and interleaved 3D spiral-projected sampling with the golden angle approach was developed.

In this paper, we aimed at developing a k-space encoding method based on spiral projection imaging (SPI) (21,22), allowing ultrashort echo time and interleaved acquisitions. This method was combined with an original sampling scheme using the golden-angle method to pseudo-randomly sample the k-space. The goal of this study was (i) to demonstrate the feasibility of ultrashort echo-time imaging using projected spiral readout; (ii) to validate that the combination with interleaves and the golden angle approach would decrease the sensitivity to T_2^* decay and enable retrospective undersampling; and (iii) to assess this new method in two different in vivo applications in mice at 7 Tesla (T).

METHODS

Magnet, Gradient System, and RF Coils

Experiments were performed on a 7T Bruker Biospec system (Ettlingen, Germany) equipped with a gradient system capable of 660 mT/m maximum strength and 110 µs rise time. A volume resonator (86-mm inner diameter, active length 70 mm) operating in quadrature mode was used for excitation, and a four-element (2 × 2) phased array surface coil (outer dimensions of one coil element: 12 × 16 mm^2, total outer dimensions: 26 × 21 mm^2) was used for signal reception.

k-Space Sampling and Trajectory

Spiral Design

Spiral trajectories were designed as previously proposed by Cline et al (23). The trajectory was defined as $\boldsymbol{k} = \boldsymbol{A\theta}.\boldsymbol{e}^{(i\boldsymbol{\theta})}$, in which A is the number of spiral arms. As proposed by Cline et al, the $\boldsymbol{\theta}(\boldsymbol{t})$ function was calculated by taking into account both the gradient amplitude (Eq. [1]) and the rate limitations (Eq. [2])

$$\theta_S(t) = \beta t^2 \left(2 + 2\left(\frac{2\beta}{3}\right)^{\frac{1}{6}} t^{\frac{1}{3}} + 2\left(\frac{2\beta}{3}\right)^{\frac{2}{3}} t^{\frac{4}{3}} \right)^{-1} \quad [1]$$

$$\theta_G(t) = \sqrt{\varphi_t^2 + 2\kappa(t - t_\tau)} \quad [2]$$

with $\beta = \frac{\gamma GD}{M}$ and $\kappa = \frac{\gamma SD}{M}$, where G is the maximum gradient intensity, S is the maximum available slew rate, φ_t is the continuous rotation angle, γ is the gyromagnetic ratio, D is the field of view, M is the number of interleaves, and t_τ is the transition point between slew rate and gradient amplitude limited domains.

3D k-Space Sampling

To generate a ball-like k-space, spiral gradients were applied along the three directions (x, y, and z). To minimize the T_2^* sensitivity induced by the long data collection, an interleave approach was developed to reduce the readout time and the number of sampled points per readout. Spiral interleaves were rotated around two axes, for example (x, z). The global aim was to produce disk-like trajectories, in which each disk contained spiral interleaves (rotated around the x axis). The 3D encoding was performed by tilting the disks (rotation around the z axis) with a golden angle. Trajectories were calculated as follows:

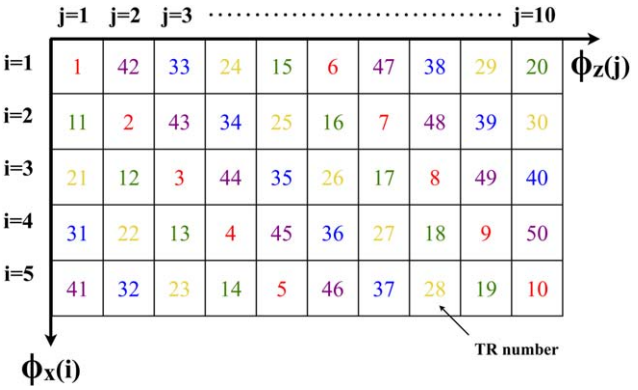

FIG. 1. Acquisition method to fill a 3D k-space using 10 disks with 5 interleaves. The colored numbers represent the TR numbers. The first acquired spiral (at TR number 1) was associated with a couple of rotation angles around the z-axis ($\phi_z(1)$) and x-axis ($\phi_x(1)$). Then, each of the following recorded spirals were associated with a different couple of rotation angles $\phi_z(j)$ and $\phi_x(i)$. The number colors match with the spiral colors in Figure 2.

$$k_x = A.\theta(t).cos(\theta(t) + \phi_x(i)) \quad [3]$$

$$k_y = A.\theta(t).sin\Big(\theta(t) + \phi_x(i)\Big).\cos(\phi_z(j)) \quad [4]$$

$$k_z = A.\theta(t).sin\Big(\theta(t) + \phi_x(i)\Big).\sin(\phi_z(j))$$

$$\phi_x(i) = \frac{2\pi}{N_{Interleave}}.i \quad \text{and} \quad \phi_z(j) = \pi.(3 - \sqrt{5}).j \quad [5]$$

The θ function was chosen as previously explained; i is a variable corresponding to the number of interleaves per disks (from 1 to $N_{interleave}$), and j is a variable that corresponds to the number of disks (from 1 to N_{disks}). Figure 1 shows an example of the k-space filling order for 10 disks of five interleaves. The first acquired spiral corresponded to the first pulse repetition time (TR) and was associated with a rotation angle around the z axis ($\phi_z(1)$) and the x axis ($\phi_x(1)$). For the following TRs, each spiral was associated with a different couple of ϕ_z and ϕ_x, and was calculated as shown in Figure 1. Figure 2 shows a 3D view of the corresponding k-space filling. The first acquired spiral (TR number 1) corresponded to the first interleave (I_1) of the first disk (D_1). Then, the second spiral (TR number 2) was associated with a second couple of angles ($\phi_z(2)$ and $\phi_x(2)$), corresponding to the second interleave (I_2) of the second disk (D_2). The use of a golden angle ($\phi_z(j)$) allowed the production of a ball-like shaped k-space in a short acquisition time (from TR number 1 to TR number 10). Then, at TR number 11, the second interleave of the first disk was acquired. This acquisition scheme was repeated until obtaining the k-space made of 10 disks of five interleaves. For each experiment, the k-space was acquired with a fixed number of 128 disks (N_{disks}) and a variable couple of number

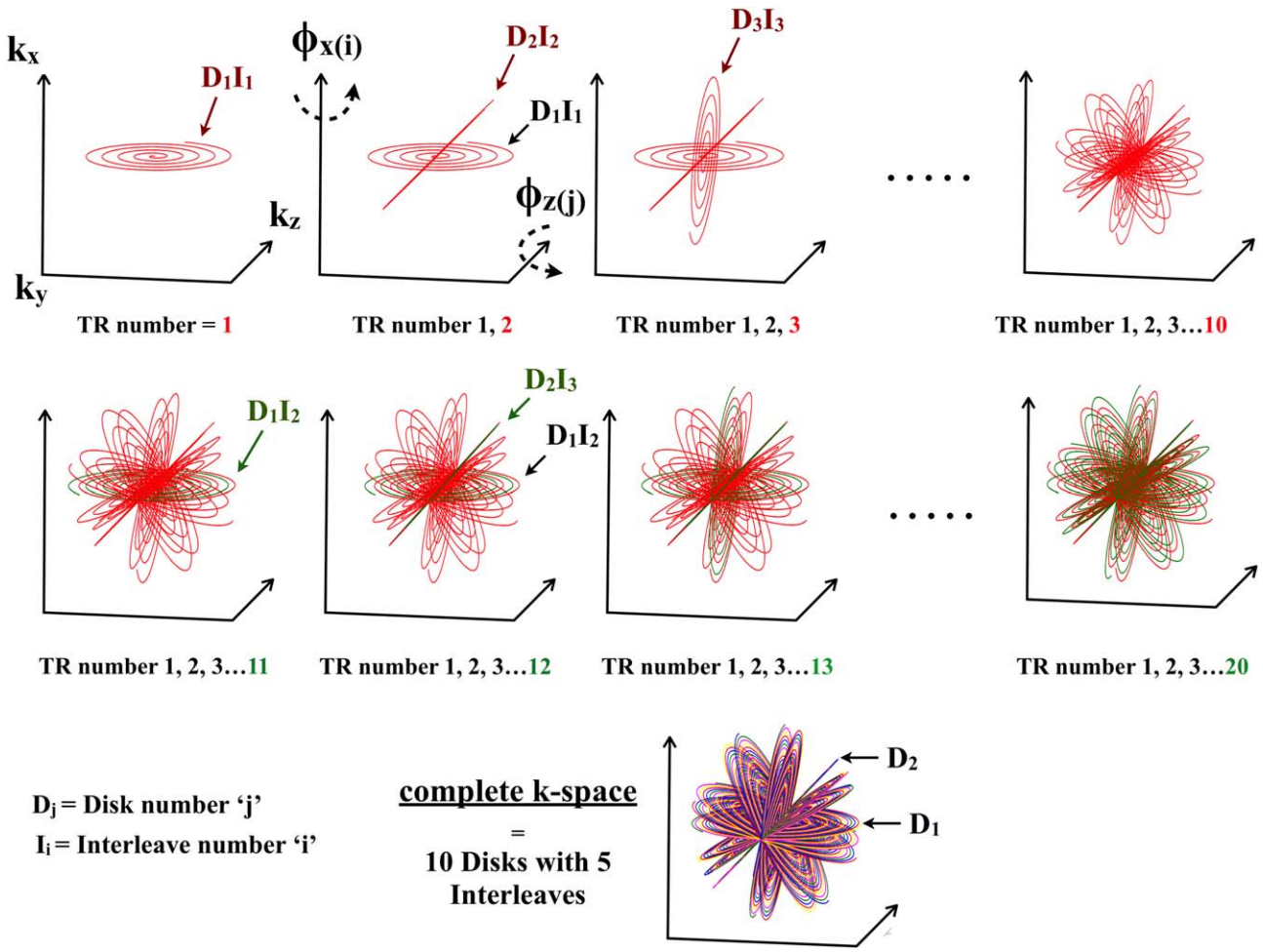

FIG. 2. Example of 3D k-space filling for 10 disks of 5 interleaves per disk. At the first TR, the first interleave (I_1) of the first disk (D_1) was recorded. Then, the next acquired spiral was rotated along the *x*-axis ($\phi_x(2)$) and *z*-axis ($\phi_z(2)$) as shown by the dashed arrows and corresponded to the second interleave (I_2) of the second disk (D_2). This acquisition was repeated to generate a ball-like complete k-space composed of 10 disks, each one containing 5 interleaves (bottom of the figure).

of interleaves and number of data points per interleave ($N_{interleaves}$ /N_{points}).

Reconstruction Process

The k-space data were regridded with an oversampling of 2 using a Kaiser-Bessel kernel (24). Final images were reconstructed by applying a fast Fourier transform (FFT). Each phased array receiver magnitude image was reconstructed using the method described previously and then combined with a sum of squares reconstruction. The reconstruction algorithm was implemented in MATLAB (The MathWorks, Natick, Massachusetts). Before the regridding, spiral trajectories were measured and averaged on a phantom filled with water to minimize the lack of signal-to-noise ratio (SNR), as presented by Beaumont et al (25). The MR signals of two slices (with three different dephasing gradient intensities) from each side of the magnet iso-center were measured. From these signals, a phase was measured for each slice. Then, the phase difference allowed for the calculation of the trajectory along the *x, y,* and *z* axis. This measurement requires 6 TR per axis for one spiral interleave. For all experiments, the trajectories were measured only for the first 128 interleaves. The whole 3D trajectory was then calculated on MATLAB and used for the regridding procedure, allowing to correct both eddy currents and the gradient delay errors.

In Vitro Experiments

Resolution Phantom

A homemade resolution phantom was built by introducing a resolution comb and a Lego wheel (Billund, Denmark) into a 10-mL syringe as shown in the Supporting Information (Supp. Figs. S1a and S1b). Then, the syringe was filled with increasing concentrations of ultrasmall superparamagnetic iron oxide (USPIO) (0, 1, 3, and 5 mM).

Imaging Parameters

For each USPIO concentration, the T_2^* decay was measured with a multigradient echo sequence using the

following parameters: TR/TE: 405/2 ms, number of echo images: 32, TE increment: 1.6 ms, RF pulse: cardinal sine 1 ms, flip angle (FA) = 30°, matrix: 128 × 128 × 128, FOV: 20 × 20 × 20 mm^3, spatial resolution: 152 × 152 × 152 μm^3, bandwidth/pixel: 781 Hz/pixel. Then, images were acquired with the developed sequence using the following parameters: TR/TE: 5/0.025 ms, RF pulse: block pulse 0.05 ms, FA = 10°, matrix: 128 × 128 × 128, FOV: 20 × 20 × 20 mm^3, spatial resolution: 152 × 152 × 152 μm^3, bandwidth/pixel: 2344 Hz/pixel, N_{disks} = 128, $N_{interleaves}/N_{points}$ = 128/480, 64/492, 32/607, and 16/1054, corresponding to readout times of 1.6, 1.6, 2.0, and 3.5 ms, respectively.

Image Analysis

Sensitivity to T_2^* decay was evaluated by measuring the sharpness for each concentration. Using MATLAB software, intensity profiles were measured at the interface between the solution and the resolution comb. The maximum and minimum intensity values across the profile boundary were determined (I_{max} and I_{min}), which corresponded to solution and plastic resolution comb intensities, respectively. Each line profile was interpolated by a factor of 10, allowing to digitally increase the spatial resolution. Next, the distance, *d*, between $0.8(I_{max}-I_{min})+I_{min}$ and $0.2(I_{max}-I_{min})+I_{min}$ across the profile was measured, and the sharpness value for that particular profile was reported as (1/d) mm^{-1}. This quantification strategy was similar to that used by Shea et al (26) and Larson et al (27).

Sensitivity to Undersampling

To evaluate the robustness against undersampling, a reference image was acquired on the same phantom as previously, filled with a solution of USPIO of 1-mM concentration. The imaging parameters were TR/TE: 5/0.025 ms, RF pulse: block pulse 0.05 ms, FA = 10°, matrix: 128 × 128 × 128, FOV: 20 × 20 × 20 mm^3, spatial resolution: 152 × 152 × 152 μm^3, bandwidth/pixel: 2344 Hz/pixel, N_{disks} = 128, $N_{interleaves}/N_{points}$ = 128/480, readout time = 1.6 ms. After acquisition, images were reconstructed using random undersampling with increasing factors (2, 4, 6, 8, and 10). For example, an undersampling factor of 8 corresponded to an image reconstructed with 12.5% of the available raw data. To quantify the sensitivity to undersampling, sharpnesses were measured on the magnitude images as previously explained.

In Vivo Experiments

Brain Imaging

To estimate the in vivo robustness of our method, images were acquired on the brain of five healthy mice (C57Bl/6, Charles River, Paris, France). All experimental procedures were approved by the Animal Care and Use Institutional Ethics Committee of Bordeaux, France (approval No. 5012032-A). The mice respiration was followed using a balloon (SA Instruments, Stony Brook, New York) fixed on the abdomen. To visualize the time-of-flight effect, a slice selection was added prior to signal acquisition, leading to an increase in TE. The following acquisition parameters were used: TR/TE = 5/1.3 ms, RF pulse = cardinal sine 1 ms, FA = 10°, matrix = 128 × 128 × 128, FOV = 20 × 20 × 20 mm^2, spatial resolution = 152 × 152 × 152 μm^3, bandwidth/pixel = 2344 Hz, N_{disks} = 128, number of interleaves per planes ($N_{interleaves}/N_{points}$) = 128/480, 64/492, 32/607, and 16/1054.

Self-Gated Liver Imaging

To apply our method on moving organs, images were acquired in the abdomen of five healthy mice. Respiration was monitored as previously explained. To detect signal fluctuations induced by breathing, the analog to digital converter (ADC) was turned on immediately after the RF pulse. By extracting the first data point from the free induction decay (FID) and by plotting its intensity as a function of acquisition time, a curve was obtained and respiration phases were identified as previously shown by Ribot et al (28). Raw data were re-ordered as a function of their position in the breathing cycle, allowing to reconstruct cine frames free of motion artifact. For these experiments, mice were injected with 100 µL of Sinerem (Guerbet, Aulnay-sous-bois, France) at 200 $\mu mol.kg^{-1}$. The following acquisition parameters were used: TR/TE = 5/0.025 ms, RF pulse = Block pulse 0.05 ms, FA = 25°, matrix = 128 × 128 × 128, FOV = 20 × 20 × 20 mm^2, spatial resolution = 152 × 152 × 152 μm^3, bandwidth/pixel = 2344 Hz, N_{disks} = 128, $N_{interleaves}/N_{points}$ = 128/492, corresponding to 16384 projections, and number of repetitions = 10. Twenty cine frames per respiration cycle were reconstructed. Because of the self-gated reconstruction, an average of 7000 projections were used per k-space to reconstruct each cine image, and the undersampling ratio was ~2.

RESULTS

T_2^* effect

Four solutions with increasing USPIO concentrations of 0, 1, 3, and 5 mM were inserted in the resolution phantom, and T_2^* were calculated as 30, 7.1, 2.6 and 1.6 ms, respectively. Figure 3 shows the representative images acquired on the resolution phantom with two different T_2^* of 30 and 1.6 ms, respectively. The white dashed arrow points at both the off-resonance effect and T_2^* sensitivity, which induce a severe blurring artifact at the interface between the resolution comb and the solution. This artifact showed the effect of longer readout time on image quality. The white arrow shows the T_2^* effect especially on the spatial resolution. For the same readout time, shortening the T_2^* induce a blurring of the Lego wheel. This T_2^* sensitivity is increased by using a longer readout time of 3.5 ms, showing that the resolution comb became hardly distinguishable when compared with longer T_2^* value. For all T_2^* values, the sharpnesses were calculated and are provided in Table 1. As expected, the sharpness decreased with shorter T_2^* values. For example, for a readout time of 1.6 ms, the sharpness was 4.2 mm^{-1} for the longest T_2^* (30 ms) and 2.4 mm^{-1} for the shortest (1.6 ms). Also, for a fixed T_2^* of

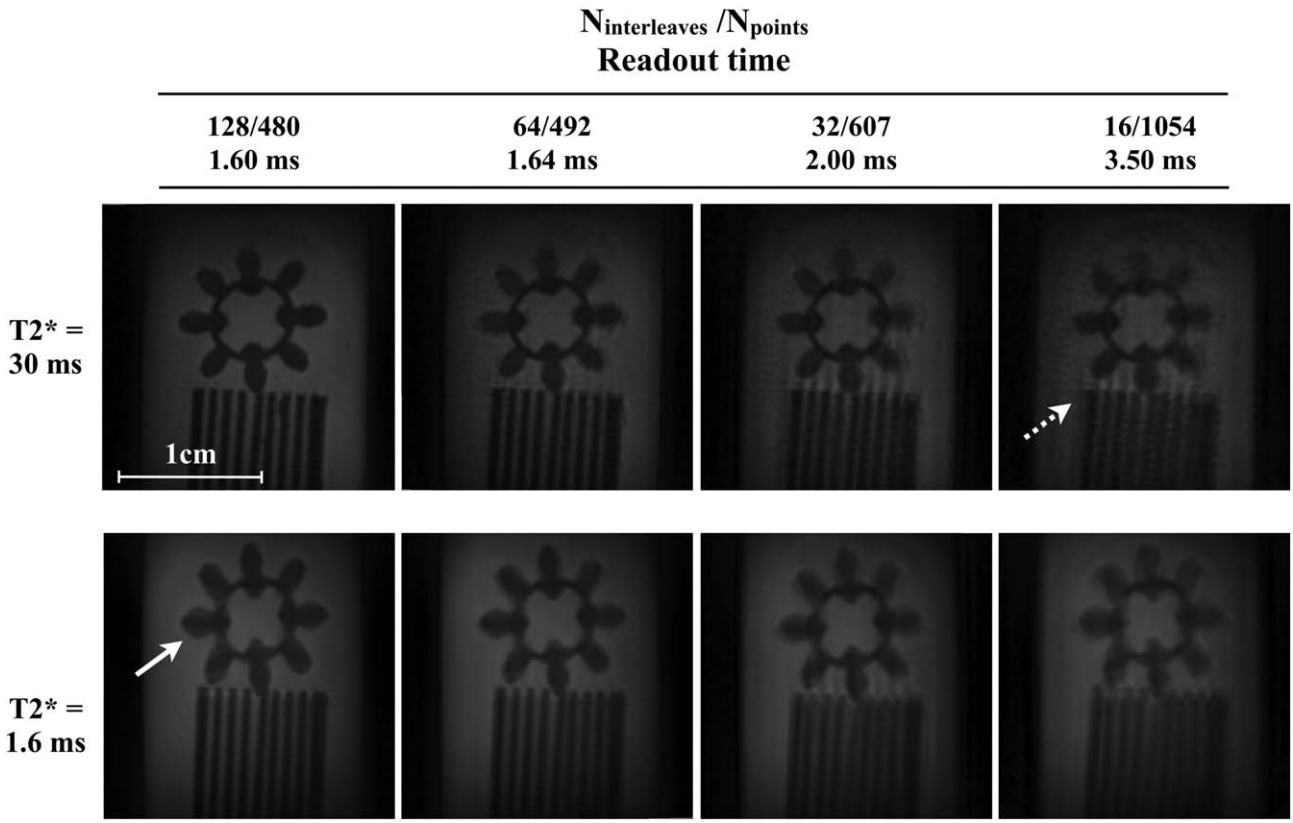

FIG. 3. Images of phantoms acquired with $N_{disks} = 128$, $N_{interleaves}/N_{points} = 128/480$, 64/492, 32/607, and 16/1054, corresponding to readout times = 1.60, 1.64, 2.00, and 3.50 ms, respectively. Two different phantoms containing two USPIO concentrations of 0 and 5 mM corresponding to $T_2^* = 30$ and 1.60 ms are shown. The dashed white arrow points at the off-resonance effect, and the white arrows point at the blurring effect induced by shorter T_2^*. Scale bar represents 1 cm.

30 ms, the sharpness was 4.2 mm^{-1} for the shortest readout time and 1.6 mm^{-1} for the longest.

Random Undersampling

Representative images using $N_{interleaves}/N_{points} = 128/492$ are shown in Figure 4. Images were acquired on a phantom containing USPIO at 1-mM concentration. Without undersampling, the resolution comb was properly visualized, and the sharpness was 4.1 mm^{-1}. The increasing undersampling ratio led to loss of spatial resolution, which was characterized by a sharpness drop from 4.1 to 1.3 mm^{-1} for the higher undersampling factor (10). For the highest undersampling ratios, streaking artifacts appeared on the magnitude images, as pointed by the white arrow in Figure 4. However, the spatial resolution is still high enough to visualize the resolution comb.

Brain Imaging

Images were acquired on healthy mice with variable $N_{interleaves}$ /N_{points}. The resulting images are shown in Figure 5. Using $N_{interleaves} = 128$ and 64, the time-of-flight effect and the spatial resolution were sufficiently high to distinguish the middle cerebral artery and its branches, as shown by the arrows in Figure 5a. With a lower number of interleaves, the middle cerebral artery could not be visualized, demonstrating the loss of spatial resolution certainly caused by off-resonance sensitivity. However, larger vessels, such as basilar arteries, could be detected regardless of the number of interleaves per disk, as shown by the dashed arrow in Figure 5b. The total scan times to acquire these 3D images were 1 min 20 s, 40 s, 20 s, and 10 s, corresponding to $N_{interleaves}/N_{points} =$ 128/480, 64/492, 32/607, and 16/1054, respectively.

Respiratory Self-Gated 3D Liver Angiography

Images were acquired on healthy awake mice breathing at 120 inspirations per min. Twenty frames were reconstructed per respiratory cycle. As shown in Figure 6, the injection of USPIO coupled with the ultrashort echo time of our sequence generated a positive contrast between the blood vessels and the liver. Moreover, after the self-gated reconstruction, the whole liver angiogram was detected (arrows) without any blurring effect caused

Table 1
Calculated Sharpness as a Function of Variable Readout Time Corresponding to Variable $N_{interleaves}$ per Disk (128, 64, 32, and 16, respectively) and Decreasing T_2^* values (30, 7.1, 2.6, and 1.6 ms)

	Sharpness/mm^{-1}			
T_2^* / ms	Readout = 1.60 ms	1.64 ms	2.00 ms	3.50 ms
30	4.2	2.7	1.8	1.6
7.1	4.1	2.4	1.4	1.3
2.6	3.4	2.3	1.3	1.2
1.6	2.4	2.2	1.2	1.1

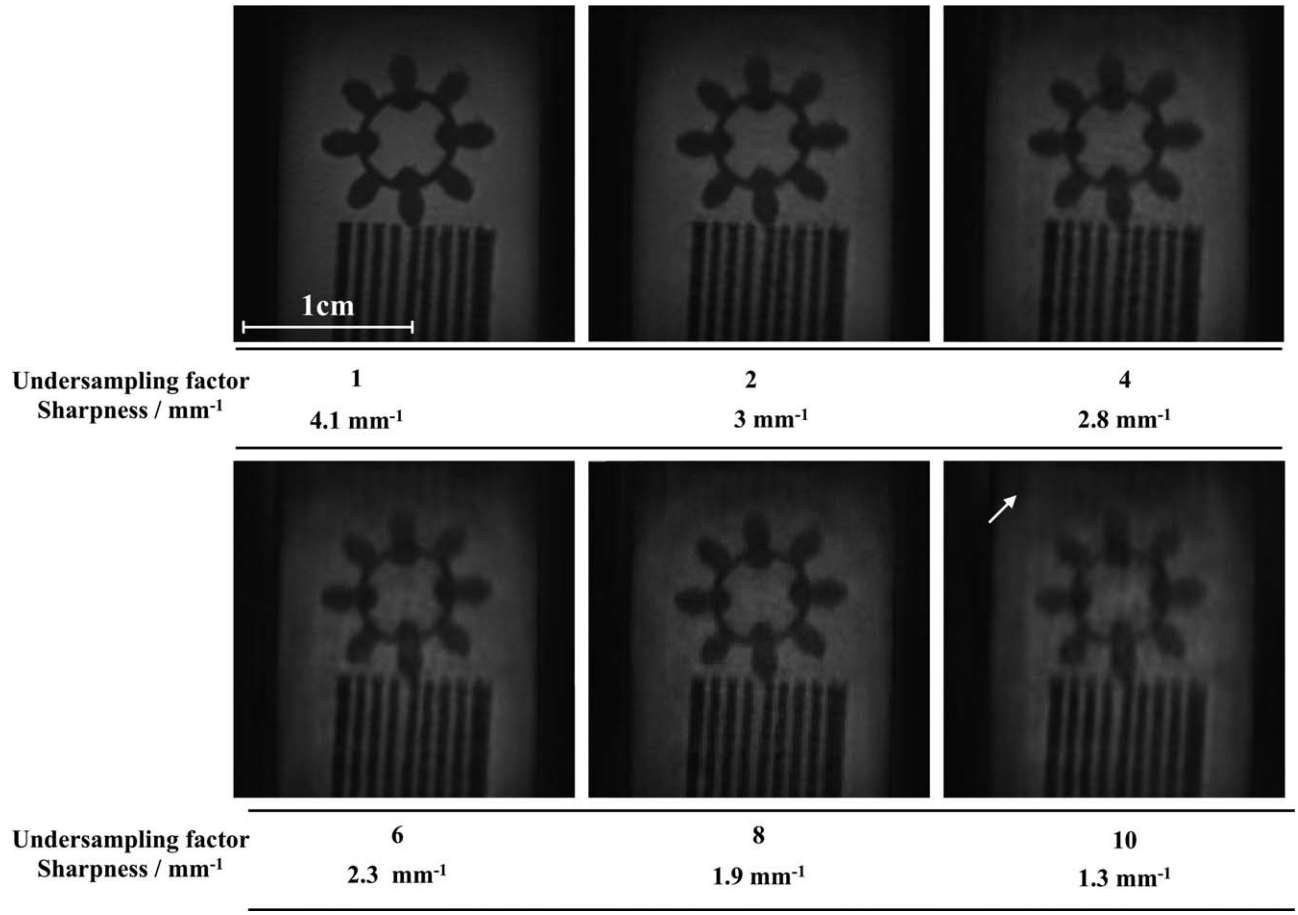

FIG. 4. Images on phantoms acquired with $N_{disks} = 128$, $N_{interleaves}/N_{points} = 128/480$, and randomly undersampled before reconstruction with increasing ratios (2, 4, 6, 8, and 10). Calculated sharpness (mm^{-1}) corresponding to each image is also shown. The white arrow points at the streaking artifact. Scale bar represents 1 cm.

by breathing. The overall acquisition time was 12 min. As previously explained, the mean number of projections per k-space was 7000, corresponding to an undersampling factor of two, as compared with the nongated reference k-space of $N_{disk} = 128$, $N_{interleaves}/N_{points} = 128/492$. The movie corresponding to the images shown in Figure 6 were added in the Supporting Information (Supporting videos S1 (axial view) and S2 (sagittal view)).

DISCUSSION

In this project, an original MRI sequence based on hybrid spiral/radial, also called *spiral projected imaging*, was developed. This method allowed ultrashort echo time and both prospective and retrospective undersampling, caused by the use of the golden-angle approach. First, the sensitivity to T_2^* and its effect on the sharpness of the images were evaluated. The robustness for undersampling was also quantified by measuring the sharpness on images reconstructed with reduced numbers of spiral projections. Then, this method was applied to mice in vivo whole brain angiography and respiratory self-gated 3D liver angiography at 7 T.

The major advantage of combining spiral and radial acquisitions versus conventional sampling strategies was the overall acquisition time reduction. By considering a 128^3 Cartesian matrix, the acquisition time is ($128 \times 128 \times TR$). For a 3D radial acquisition, this acquisition time is increased by a factor π leading to ($\pi \times 128 \times 128 \times TR$) according to the Nyquist criterion (29). Using a spiral sampling can significantly reduce the scan time by playing with several parameters such as the number of disks (N_{Disks}) and the number of interleaves ($N_{interleaves}$). In this case, the acquisition time can be expressed as ($N_{Disks} \times N_{Interleaves} \times TR$). Because N_{Disks} was fixed to 128 for all experiments, the acquisition time depends only on the number of interleaves per disk. In vitro experiments showed the possibility of decreasing $N_{interleaves}$ up to 16, allowing the reduction of acquisition time by a factor of 8 and 25 when compared with Cartesian and radial sampling, respectively, without using parallel imaging or compressed sensing (CS) reconstruction. The second advantage of this approach was the k-space center oversampling. Indeed, each spiral was registered from the center to the peripheral parts of the k-space, allowing the motion sensitivity to decrease while increasing the SNR. Moreover, such an encoding scheme did not require the use of an additional Cartesian encoding in the third direction, allowing maximal TE reduction. Both the oversampling of the k-space center (30) and the ultrashort echo time (31) allowed by this method led to a decrease in sensitivity to blood flow, particularly

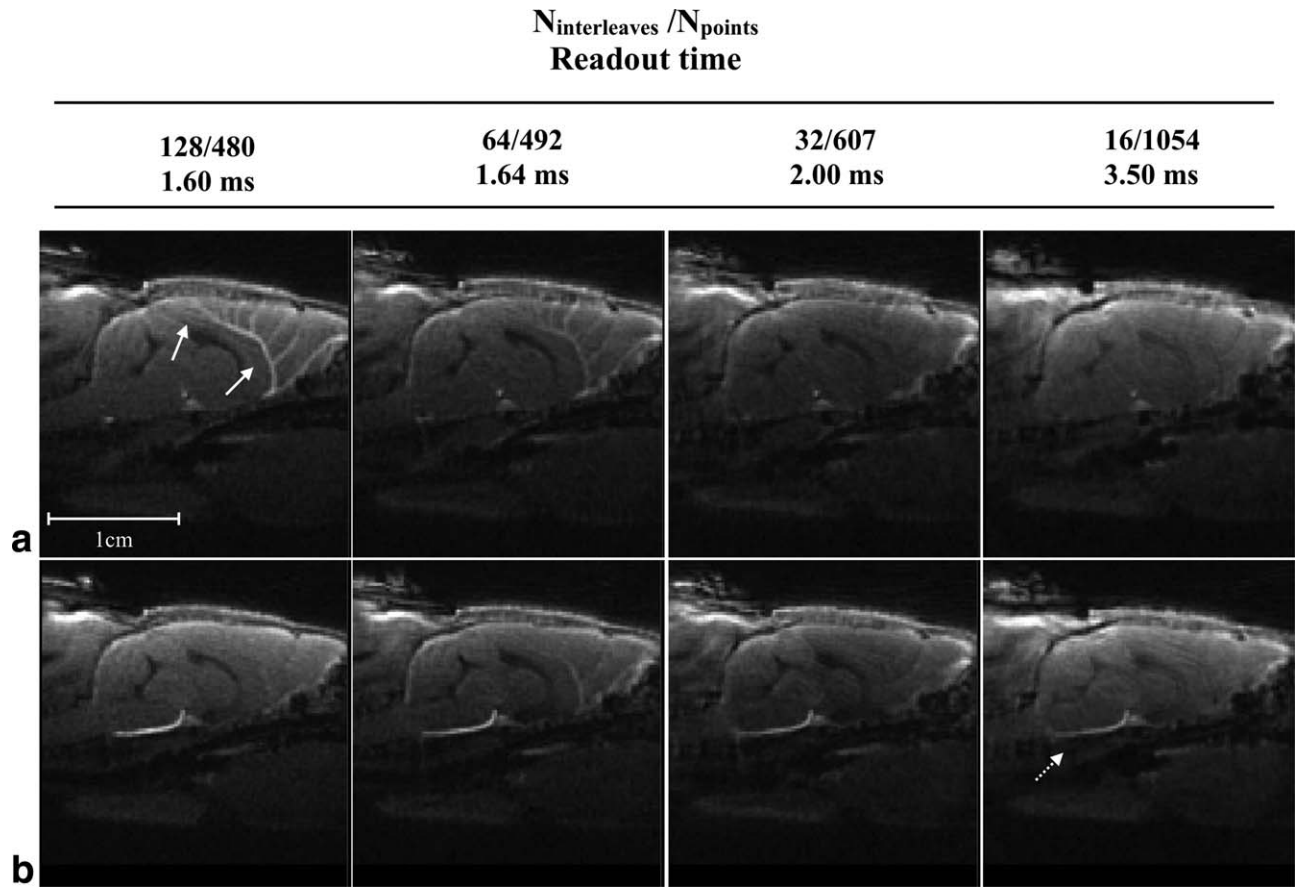

FIG. 5. Sagittal brain images acquired on a healthy mouse with variable $N_{interleaves}/N_{points} = 128/480$, 64/492, 32/607, and 16/1054. The rows (a, b) represent the two different slices. The white arrows point at the cerebral middle artery. The dashed arrow points at the basilar artery. Scale bar represents 1 cm.

for small animal angiography. Few methods similar to spiral projected imaging (SPI), namely, cones and twisted projections, enabled the oversampling of the center of the k-space. These methods have been used previously to quantify short T_2^* nucleus, such as sodium, in both brain and cartilage (13,16). However, none of these techniques were applied on the abdomen, an area that is strongly affected by motion. In this paper, after demonstrating that, even at high concentration of USPIO, no distortion or severe blurring artifact affected the in vitro images. The interest of combining UTE, USPIO injection, and spiral projected imaging was demonstrated for 3D respiratory self-gated liver angiography. As shown in Figure 6, blood vessels were visualized with a positive contrast without flow artifact. All of these results showed an interest in using this method for abdominal imaging, which is a major challenge in small animals. Potential applications on lung and osteo-articular imaging should also be considered.

Coupling SPI protocol with the golden-angle approach also allowed the use of both prospective and retrospective undersampling. Indeed, this encoding strategy allowed undersampling in both radial (by removing spiral interleaves in a given disk) and azimuthal (by recording less disks) directions. The robustness for undersampling was first demonstrated in vitro. Even with an undersampling factor of 10 (meaning that 90% of raw data were removed for image reconstruction), the sharpness only decreased by a factor of three. This result was validated in vivo with a self-gated reconstruction of a 3D mouse liver angiography, which was performed using a random undersampling (in both radial and azimuthal direction). This intrinsic robustness to undersampling made it possible to consider dynamic applications such as first-pass perfusion imaging as well as motion correction for abdominal investigations. Further experiments are currently in progress to investigate the ability of combining sliding window reconstruction with the SPI method developed in this study. Moreover, several techniques were recently proposed in the literature for combining twisted projection (32) and spiral (33) with both parallel imaging and a compressed sensing algorithm. Coupling SPI to powerful reconstruction procedures should allow very fast data collection and image reconstruction. Several technical issues should be taken into account for combining CS with the imaging protocol proposed in this paper. Indeed, as mentioned by Tolouee et al (34) and Feng et al (35), the spatio-temporal sparsity of the acquired data is of great importance for CS reconstruction using spiral and radial samplings. Although the use of golden angle between each disk allowed us to pseudo-randomly fill the ball-shaped k-space, the use of a second golden angle between each spiral interleave should be considered and the effect on the CS

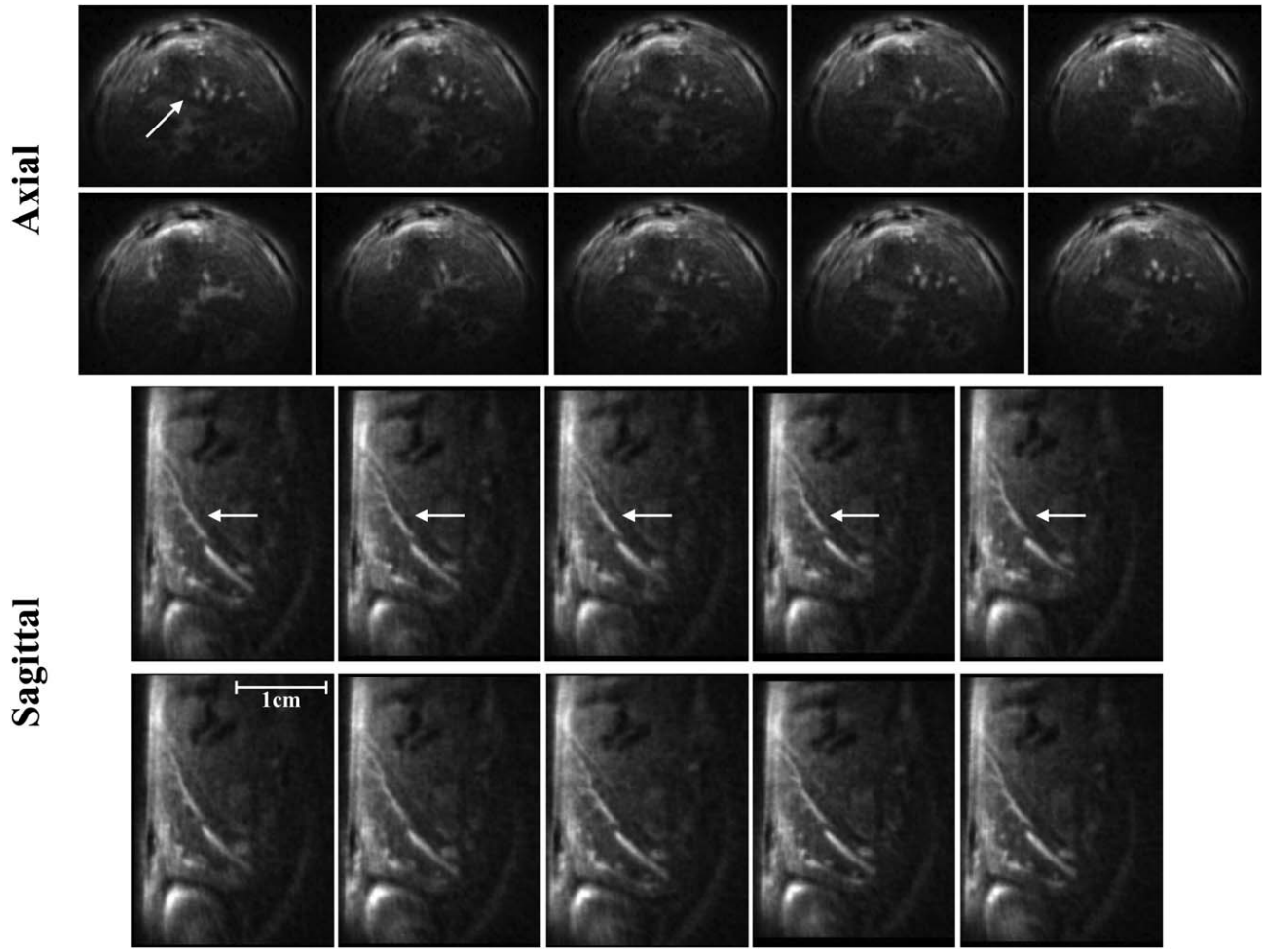

FIG. 6. Self-gated 3D liver angiography (axial and sagittal views). Each extracted image represents a cine frame synchronized with breathing. The white arrows point at regions of interest that move during the breathing cycle (inspiration and expiration). The corresponding films were added in the Supporting Information. Scale bar represents 1 cm.

reconstruction be evaluated. Moreover, the sampling strategy used for dynamic applications such as the free-breathing liver angiography presented here will also have to be modified to optimize the data sparsity through time, as proposed by Tolouee et al (34). Although the combination of this imaging protocol with CS should enable a more aggressive undersampling regime, this will require further investigations to take full advantage of this new flexible acquisition strategy.

Although this method showed promising results in vitro and in vivo, several issues still remain. First, the longer readout time generated by spiral acquisition is double-edged, especially at high magnetic field when compared with conventional fast Cartesian methods, radial sampling and echo-planar imaging. In truth, it allows fast data collection, but the resulting images may suffer from severe blurring artifact. In this paper, a combination of high bandwidth (300 kHz) and an interleaved approach limited this artifact. Furthermore, the longer T_2^* observed at lower magnetic field (1.5 T) may lead to faster signal acquisition by significantly reducing the number of interleaves per disk. The second limitation related to the use of spiral readout was the sensitivity to off-resonance and chemical shift artifacts, which should be taken care of in further investigations in the abdomen. Several methods have already been developed to suppress fat signal contribution on both clinical (36) and preclinical scanners (37) and may be easily combined with the sampling strategy as proposed in this project. The third drawback of the SPI method was related to the trajectories themselves. Indeed, to obtain a ball-like k-space, the gradients were activated in the three directions (x, y, and z), which may lead to trajectory errors caused by eddy currents and gradient delay approximations. To correct such errors, trajectories were measured before the signal acquisition and used during the regridding procedure. This measurement protocol presents two main drawbacks. The first is the lack of signal that may disturb the trajectory measurement. To overcome this drawback, the measurement of the first spiral interleaves was made on phantom with four averages. The second limitation is caused by the spiral design itself. Each time the number of points per spiral, spirals per disk, or readout bandwidth changed, a new trajectory measurement was necessary. This procedure may be time-consuming. However, because all measurements were made on phantom, this was not a limiting factor for in vivo experiments. Finally, even though isotropic FOV required for

signal acquisition may be an advantage for whole body applications, it can be a limiting factor for imaging restricted body areas. However, a previously developed method could then be applied on this sampling strategy to acquire anisotropic FOV (38).

The acquisition protocol established in this work displayed interesting features especially in terms of acquisition time, robustness for undersampling, and flexibility caused by spiral gradients. Spiral readout can be either in or out, allowing variations of the echo-time values leading to potential applications for fMRI studies. Recent works demonstrated interest in using fast spiral acquisitions for such applications (39,40). But, as far as we know, no spiral projected imaging for fMRI has yet been reported in the literature. Moreover, the ability to switch from very short to very long echo times would represent a great advantage for measuring in vivo temperature using phase image differences. The use of 2D spiral acquisition for this kind of application has already been discussed by Stafford et al (41). However, it should be very interesting to monitor temperature variations in 3D, and we believe that the proposed method provides sufficient flexibility and robustness to properly retrieve this information. Finally, the fast 3D k-space sampling enabled by this acquisition strategy may have implications in 3D real-time imaging. The usefulness of spiral trajectories has already been demonstrated for 2D imaging in applications such as real-time bSSFP heart imaging (42) and for distortion correction (43). However, no method allowing 3D real-time imaging has been proposed in the literature yet. This could have major implications, especially on applications such as catheter tracking (44).

CONCLUSIONS

In this study, an innovative method based on spiral projection imaging coupled with a golden-angle approach and ultrashort echo time has been proposed. The robustness for undersampling and the sensitivity to short T_2^* were evaluated in both in vitro and in vivo experiments. This protocol was validated for 3D angiography on both mouse brain and liver. The ultrashort echo time combined with the high robustness for undersampling would be a major asset to this sequence in a wide range of applications in which flexibility and short acquisition time are needed.

ACKNOWLEDGMENTS

This work was supported by a public grant, Translational Research and Advanced Imaging Laboratory, which is part of the French National Research Agency's Investments for the Future Program ("NewFISP"; ANR-10-LABX-57).

REFERENCES

1. Ahn CB, Kim JH, Cho ZH. High-speed spiral-scan echo planar NMR imaging-I. IEEE Trans Med Imaging 1986;5:2–7.
2. Meyer CH, Hu BS, Nishimura DG, Macovski A. Fast spiral coronary artery imaging. Magn Reson Med 1992;28:202–213.
3. Glover GH. Spiral imaging in fMRI. NeuroImage 2012;62:706–712.
4. Yang PC, Meyer CH, Terashima M, Kaji S, McConnell MV, Macovski A, Pauly JM, Nishimura DG, Hu BS. Spiral magnetic resonance coronary angiography with rapid real-time localization. J Am Coll Cardiol 2003;41:1134–1141.
5. Castets CR, Ribot EJ, Lefrançois W, Trotier AJ, Thiaudière E, Franconi JM, Miraux S. Fast and robust 3D T1 mapping using spiral encoding and steady RF excitation at 7 T: application to cardiac manganese enhanced MRI (MEMRI) in mice. NMR Biomed 2015;28:881–889.
6. Shin, Taehoon, Michael Lustig, Dwight G. Nishimura, Bob S. Hu. Rapid single-breath-hold 3D late gadolinium enhancement cardiac MRI using a stack-of-spirals acquisition. J Magn Reson Imaging 2014; 40:1496–1502.
7. Pierce, Iain T., Jennifer Keegan, Peter Drivas, Peter D. Gatehouse, David N. Firmin. Free-breathing 3D late gadolinium enhancement imaging of the left ventricle using a stack of spirals at 3T. J Magn Reson Imaging 2015;41:1030–1037.
8. Yongxian Q, Zhao T, Zheng H, Weimer J, Boada FE. High-resolution sodium imaging of human brain at 7 T. Magn Reson Med 2012;68: 227–233.
9. Boada FE, Shen GX, Chang SY, Thulborn KR. Spectrally weighted twisted projection imaging: reducing T_2 signal attenuation effects in fast three-dimensional sodium imaging. Magn Reson Med 1997;38: 1022–1028.
10. Thulborn KR, Davis D, Adams H, Gindin T, Zhou J. Quantitative tissue sodium concentration mapping of the growth of focal cerebral tumors with sodium magnetic resonance imaging. Magn Reson Med 1999;41:351–359.
11. Borthakur A, Hancu I, Boada FE, Shen GX, Shapiro EM, Reddy R. In vivo triple quantum filtered twisted projection sodium MRI of human articular cartilage. J Magn Reson 1999;141:286–290.
12. Boada F, Gillen J, Shen G, Chang S, Thulborn K. Fast three dimensional sodium imaging. Magn Reson Med 1997;37:706–715.
13. Staroswiecki E, Bangerter NK, Gurney PT, Grafendorfer T, Gold GE, Hargreaves BA. In vivo sodium imaging of human patellar cartilage with a 3D cones sequence at 3 T and 7 T. J Magn Reson Imaging 2010; 32:446–451.
14. Wu HH, Gurney PT, Hu BS, Nishimura DG, McConnell MV. Free-breathing multiphase whole-heart coronary MR angiography using image-based navigators and three-dimensional cones imaging. Magn Reson Med 2013;69:1083–1093.
15. Yongxian Q, Boada FE. Acquisition-weighted stack of spirals for fast high-resolution three-dimensional ultra-short echo time MR imaging. Magn Reson Med 2008;60:135–145.
16. Riemer F, Solanky BS, Stehning C, Clemence M, Wheeler-Kingshott CAM, Golay X. Sodium (23Na) ultra-short echo time imaging in the human brain using a 3D-cones trajectory. MAGMA 2014;27:35–46.
17. Konstavsndin S, Krämer P, Günther M, Schad LR. Sodium magnetic resonance imaging using ultra-short echo time sequences with anisotropic resolution and uniform k-space sampling. Magn Reson Imaging 2015;33:319–327.
18. Winkelmann S, Schaeffter T, Koehler T, Eggers H, Doessel O. An optimal radial profile order based on the golden ratio for time-resolved MRI. IEEE Trans Med Imaging 2007;26:68–76.
19. Wundrak S, Paul J, Ulrici J, Hell E, Rasche V. A small surrogate for the golden angle in time-resolved radial MRI based on generalized Fibonacci sequences. IEEE Trans Med Imaging 2015;34:1262–1269.
20. Turley DC, Pipe JG. Distributed spirals: a new class of three-dimensional k-space trajectories. Magn Reson Med 2013;70:413–419.
21. Irarrazabal P, Nishimura DG. Fast three dimensional magnetic resonance imaging. Magn Reson Med 1995;33:656–662.
22. Pipe JG, Koladia KV. Spiral projection imaging: a new fast 3D trajectory. In: Proceedings of the 13th International Society of Magnetic Resonance in Medicine Meeting, Miami Beach, FL, 2005; Abstract 2402.
23. Cline HE, Zong X, Gai N. Design of a logarithmic k-space spiral trajectory. Magn Reson Med 2001;46:1130–1135.
24. Beatty PJ, Nishimura DG, Pauly JM. Rapid gridding reconstruction with a minimal oversampling ratio. IEEE Trans Med Imaging 2005;24: 799–808.
25. Beaumont M, Lamalle L, Segebarth C, Barbier EL. Improved k-space trajectory measurement with signal shifting. Magn Reson Med 2007; 58:200–205.
26. Shea SM, Kroeker RM, Deshpande V, Laub G, Zheng J, Finn JP, Li D. Coronary artery imaging: 3D segmented k-space data acquisition with multiple breath-holds and real-time slab following. J Magn Reson Imaging 2001;13:301–307.

27. Larson AC, Kellman P, Arai A, Hirsch GA, McVeigh E, Li D, Simonetti OP. Preliminary investigation of respiratory self-gating for free-breathing segmented cine MRI. Magn Reson Med 2005;53:159–168.
28. Ribot EJ, Duriez TJ, Trotier AJ, Thiaudiere E, Franconi JM, Miraux S. Self-gated bSSFP sequences to detect iron-labeled cancer cells and/or metastases in vivo in mouse liver at 7 Tesla. J Magn Reson Imaging 2015;41:1413–1421.
29. Bernstein MA, King KF, Zhou XJ. Handbook of MRI pulse sequences. Burlington, MA, Elsevier Academic Press, 2004.
30. Trotier AJ, Lefrançois W, Ribot EJ, Thiaudiere E, Franconi JM, Miraux S. Time-resolved TOF MR angiography in mice using a prospective 3D radial double golden angle approach. Magn Reson Med 2015;73:984–994.
31. Hoerr V, Nagelmann N, Nauerth A, Kuhlmann MT, Stypmann J, Faber C. Cardiac-respiratory self-gated cine ultra-short echo time (UTE) cardiovascular magnetic resonance for assessment of functional cardiac parameters at high magnetic fields. J Cardiovasc Magn Reson 2013;15:59.
32. Addy NO, Ingle RR, Wu HH, Hu BS, Nishimura DG. High-resolution variable-density 3D cones coronary MRA. Magn Reson Med 2015;74: 614–621.
33. Dyvorne H, Knight-Greenfield A, Jajamovich G, Besa C, Cui Y, Stalder A, Markl M, Taouli B. Abdominal 4D flow MR imaging in a breath hold: combination of spiral sampling and dynamic compressed sensing for highly accelerated acquisition. Radiology 2015; 275:245–254.
34. Tolouee A, Alirezaie J, Babyn P. Compressed sensing reconstruction of cardiac cine MRI using golden angle spiral trajectories. J Magn Reson 2015;260:10–19.
35. Feng L, Grimm R, Block KT, Chandarana H, Kim S, Xu J, Axel L, Sodickson DK, Otazo R. Golden-angle radial sparse parallel MRI: combination of compressed sensing, parallel imaging, and golden-angle radial sampling for fast and flexible dynamic volumetric MRI. Magn Reson Med 2014;72:707–717.
36. Börnert P, Koken P, Eggers H. Spiral water-fat imaging with integrated off-resonance correction on a clinical scanner. J Magn Reson Imaging 2010;32:1262–1267.
37. Ragan DK, Bankson JA. Two-point Dixon technique provides robust fat suppression for multi-mouse imaging. J Magn Reson Imaging 2010;31:510–514.
38. Larson PZ, Gurney PT, Nishimura DG. Anisotropic field-of-views in radial imaging. IEEE Trans Med Imaging 2008;27:47–57.
39. Glover GH. Spiral imaging in fMRI. NeuroImage 2012;62:706–712.
40. Jung Y, Samsonov AA, Liu TT, Buracas GT. High efficiency multishot interleaved spiral-in/out: acquisition for high-resolution BOLD fMRI. Magn Reson Med 2013;70:420–428.
41. Stafford RJ, Hazle JD, Glover GH. Monitoring of high-intensity focused ultrasound-induced temperature changes in vitro using an interleaved spiral acquisition. Magn Reson Med 2000;43:909–912.
42. Feng X, Salerno M, Kramer CM, Meyer CH. Non-Cartesian balanced steady-state free precession pulse sequences for real-time cardiac MRI. Magn Reson Med 2015;75:1546–1555.
43. Campbell-Washburn AE, Xue H, Lederman RJ, Faranesh AZ, Hansen MS. Real-time distortion correction of spiral and echo planar images using the gradient system impulse response function. Magn Reson Med 2015. doi: 10.1002/mrm.25788.
44. Whiting N, Hu J, Shah JV, Cassidy MC, Cressman E, Zacharias MN, Menter DG, Marcus CM, Bhattacharya PK. Real-time MRI-guided catheter tracking using hyperpolarized silicon particles. Sci Rep 2015;5:12842.

SUPPORTING INFORMATION

Additional Supporting Information may be found in the online version of this article

Supporting Figure S1. (a) Homemade resolution phantom composed of a 10-mL syringe with two plastic pieces. Magnified in (b), the resolution phantom is composed of a resolution comb (black arrow) and a Lego wheel (white arrow).
Supporting Video S1. Movie presenting an axial view of the liver of a breathing mouse without respiratory gating.
Supporting Video S2. Movie presenting a sagittal view of the liver of a breathing mouse without respiratory gating.